Visualizing flow vortices inside a single levitated drop

A. Amar [a,*], E. Groß-Hardt [b], A.A. Khrapitchev [a], S. Stapf [a], A. Pfennig [b], B. Blümich [a]

[a] *Institute of Technical and Macromolecular Chemistry, ITMC, RWTH Aachen, Worringerweg 1, D-52074 Aachen, Germany*
[b] *Department of Chemical Engineering/Thermal Unit Operations, TVT, RWTH Aachen, Wüllnerstr. 5, D-52062 Aachen, Germany*

Abstract

The internal flow dynamics in single liquid drops, kept in place through levitation by a counterflowing continuous fluid phase in a suitably designed glass cell, is investigated by PFG NMR techniques. The positional stability of the drops was confirmed from series of one-dimensional profiles and was found to be below the spatial resolution of the experiment. Velocity distribution functions (propagators) along all three coordinates were obtained and demonstrated the long-time stability of the internal dynamics in terms of the velocity magnitudes occurring in the systems. Finally, velocity imaging was applied to visualize the internal vortex patterns in the drops either as projections onto different planes or within thin slices of selected orientations. Two different fluid systems were investigated in order to cover the principal cases of rigid and mobile interfaces. Different fast velocity imaging techniques were employed for monitoring the vastly differing velocity ranges of both cases, and the high sensitivity of the internal three-dimensional motion to the cell geometry is demonstrated.
© 2005 Elsevier Inc. All rights reserved.

Keywords: Velocity imaging; Fluid dynamics; PFG NMR; Propagator; Vortices

1. Introduction

Liquid–liquid extraction processes are of widespread use in chemical engineering and have their most important application in cleaning procedures where contaminants in a bulk, valuable fluid component (donator phase) are being removed by bringing it into contact with a second, disperse phase (acceptor phase). Ideally, donator and acceptor phase are immiscible, while the contaminant (transfer phase) is soluble in both fluids. To provide maximum transfer within a given amount of time, a large concentration difference of the contaminant and a large interface area between the two main phases are desired. This is often realized by dispersing the acceptor phase into a swarm of droplets and allowing it to pass through the continuous phase exploiting the density differences between phases.

It is a well-known fact that the efficiency of mass-transfer between the two phases is determined by convective transport made possible through circulation occurring both inside and outside of the droplets. Mass-transfer can be, in fact, substantially faster than would be expected from pure diffusive transport across the drop interface. Mass-transfer rates are underestimated by orders of magnitude by the analytical solution of Kronig and Brink [1], but also by 2D-axisymmetric CFD simulations for non-deformable droplets with an ideally mobile interfacial region, which do not make use of approximated solutions of the Navier Stokes equations [2,3]. Modelling mass-transfer, however, depends on a precise knowledge of the fluid dynamics inside the drop, which in turn can be understood theoretically only by taking into account sufficiently detailed models of the boundary layer properties. The single-droplet behaviour, which needs to be understood as a basis for the extraction-column design, is determined by mass-transfer and sedimentation, which take place

---
* Corresponding author. Fax: +49 241 80 22185.
 E-mail address: aamar@mc.rwth-aachen.de (A. Amar).

simultaneously and influence each other. Although in the past, several theoretical, numerical, and experimental investigations on single droplets have been carried out, sedimentation velocities and mass-transfer rates cannot be predicted a priori; experimental data can only be matched by additional empirical parameters. The only experimental evidence for fluid dynamics is usually delivered from integral measurements of the mass-transfer in an extraction column or in single-drop cells [4,5]. Although particle tracer methods have been used to visualize the flow pattern in drops directly [6–8], these are limited in their applicability with respect to resolution and dimensionality, frequently monitoring only motion in suitable sections within the drop. Furthermore, they represent an invasive technique which can compromise the validity of the results derived about the fluid flow field. For instance, it is known that the fluid dynamics of the drop can be very sensitive to small concentrations of impurities in the system which tend to accumulate at the interface.

Pulsed field gradient (PFG) NMR appears to be an exceptionally suitable technique for non-invasively monitoring the drop's internal fluid dynamics and its change with time. In recent literature, the versatility of velocity encoded imaging and its applicability to model systems and problems from the field of chemical engineering were demonstrated. Methods based on conventional imaging are often prohibitively slow to achieve sufficient spatial resolution in a reasonable experimental time which is required to monitor processes that are potentially instationary (see the compilation about flow NMR in [9]). Therefore, several attempts were made to combine multi-pulse and/or multi-acquisition imaging techniques with velocity encoding modules. While a long lifetime of the signal and a comparatively slow motion favours repeated refocusing as achieved by turbo spin echo/RARE [10] or EPI [11], gradient-recalled echo techniques following small flip angles as in FLASH [12] appear more appropriate if the signal lifetime is short. Sederman et al. [13] have demonstrated the feasibility of fast imaging in combination with velocity encoding to visualize transient phenomena and to determine spatially resolved velocity autocorrelation functions. However, their spatial resolution was optimized to fit the comparatively large size of the sample under study. Several more recent approaches to systems of different requirements have tackled the problem of combining high-resolution velocity measurements with fast imaging techniques [14–21]. In [22], velocities inside a small (3.5 mm) falling water drop were visualized, but with rather long experimental times due to the need to accumulate the desired information from a sufficient number of free falling individual drops.

In the present study, levitated single drops inside a continuous, liquid phase were investigated. They were kept in place by adjusting the counter current of the continuous phase in a suitably shaped device that is located inside the magnet bore; this apparatus is briefly introduced in Section 2.1. The drops of typically 2–4 mm in diameter held in this set-up had to be imaged with sufficient spatial resolution. The internal dynamics of the drops can generally be divided into different regimes. While small droplets sediment like rigid spheres, larger droplets feature pronounced internal dynamics; with knowing the properties of the substances the diameter of transition between these limiting cases can be estimated by the purely empiric 'Bond criterion.' A better indicator are measured sedimentation velocities in comparison to the CFD-simulations of the limiting cases with a mobile or a rigid interfacial region. It is one purpose of this study to discuss these limiting cases, which requires the determination of either very small or very large velocities in an otherwise identical geometry. The fact that the drops did not move as a whole allowed the application of multiple acquisition techniques, being compromised only by the need to allow full relaxation of the spin system by introducing sufficient delays in between signal encodings, contrary to the conditions in [22].

Empirical estimates do exist for predicting the dynamic properties of drops, but do require ideal systems of sufficient purity. In reality, the transition between rigid and mobile interfaces is smooth and the precise properties of the boundary are not known in detail. To discuss clearly distinct cases, two types of liquids were used as the disperse phase, namely a low-molecular weight silicone oil (octamethylcyclotetrasiloxane, OMCTS) and toluene. Small (2 mm) OMCTS drops and large (4 mm) toluene drops were generated in order to compare the limiting conditions of rigid and mobile drop interfaces. The varying ranges of velocities encountered with these systems made necessary the application of two different PFG techniques. In the experimental part of this paper, the results of stability tests by means of spin-density imaging of the drop are presented, followed by a discussion of the velocity distribution in terms of statistical measures as well as velocity maps in different spatial directions.

2. Experimental

2.1. Set-up of the levitating device

The foremost requirement for measuring internal dynamics in levitated drops is the generation of a drop being stable in position and shape for long periods of time, at least on scales below the desired resolution in the spatial and velocity dimensions. Furthermore, reproducibility of drop generation and position are needed for measurements of series of drops. A set of conical glass cells was manufactured with different geometrical parameters and degrees of skewness; some cells were

purposely made with a bent, non-vertical flow path in order to demonstrate the influence of transverse flow components of the continuous phase on the drop behaviour. One particular, perfectly symmetric cell was manufactured at Lehrstuhl für Thermische Verfahrenstechnik TVT, RWTH Aachen, that provided optimal conditions for generating and visualizing symmetric flow conditions for the case of toluene, and at the same time could fit in the NMR microimaging device. The geometry of this cell follows the experiences from a geometry optimization with the objective to maximize the stability of droplet position [23].

The experiments were conducted as follows: first, all components of the system being in contact with either liquid were thoroughly cleaned to minimize detrimental effects on the drop boundary mobility. This included glass parts, Teflon pipes and connectors as well as the pump head itself. Fig. 1 shows a schematic sketch of the principal components of the set-up: a pump maintains a constant flow of the continuous phase, which was chosen to be D_2O in order to avoid background signal contributions as much as possible. The flow occurs from top to bottom in the glass cell in order to compensate the buoyancy of the drop which is lighter than D_2O. A computer-controlled dosimeter introduces a drop of a pre-defined volume and initial speed that guarantees separation from the pipette tip. The drop rises to the
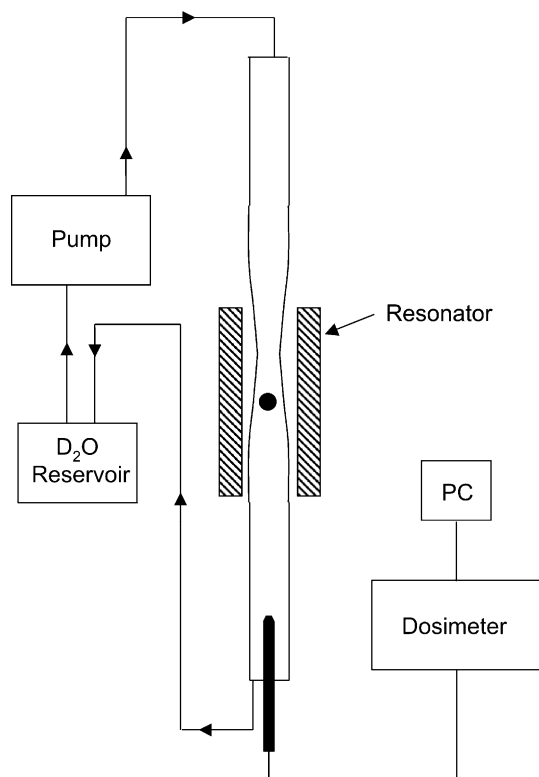
point in the narrowing section of the glass cell where all vertical forces add up to zero and the drop comes to rest; in initial experiments, the cell had been positioned vertically such that this point coincides with the centre of the resonator. It took several minutes for the drop to reach this position with a constant pump flow rate; by adjusting the pump setting manually (i.e., by allowing the drop to rise for a previously determined time and then switching on the pump), this time could be reduced to about 20 s, making this the earliest possible starting point for the NMR acquisition. Time is a critical factor inasmuch for unclean systems, the accumulation of impurities at the drop interface was found to affect its mobility within a time frame of minutes.

Before NMR experiments were started, drops of different sizes were generated outside the magnet and checked visually. It turned out that small drops could generally be levitated with no optically detectable motion, while particularly large drops sometimes appeared to undergo a weakly damped or even undamped oscillation of their vertical position. The positional stability of the drop was verified with 1D frequency encoded imaging each time before performing the velocity-sensitive experiments (see below).

2.2. Samples and hardware

Two different fluids were investigated in order to access the limiting cases of immobile and mobile interfaces. In both systems, D_2O was used as the continuous phase; D_2O was purchased from Aldrich with a degree of deuteration of 99.8%. System I used octamethylcyclotetrasiloxane, OMCTS (Fluka) with 99% purity as the disperse phase. OMCTS possesses a density of 0.956 gcm^{-3}. Small OMCTS drops were chosen as they represent a case of nearly immobile interface relative to D_2O. The drop diameters were in the range 2–3 mm. In system II, toluene (Aldrich, 99.5% purity, density 0.867 gcm^{-3}) was chosen as the drop phase. Water, toluene, and acetone as the transfer component is a typical test case for laboratory investigations of extraction and sedimentation processes; from this experience it is known that enhanced mass-transfer can be observed for relatively large drops, indicating a mobile interface. To this end, toluene drops of about 4 mm diameter were used, while larger ones became unstable in the cell nozzle or tended to touch the glass wall due to their pronounced oscillations. For both OMCTS and toluene, the D_2O phase had been presaturated with the disperse phase prior to the experiments by standard methods (shaking of a container filled with both liquids and awaiting complete phase separation).

NMR experiments discussed in this work were conducted on two different instruments, at 4.7 T field strength (200 MHz ^{1}H Larmor frequency) equipped with a Bruker DSX 200 spectrometer, and at 11.7 T field

Fig. 1. Schematic sketch of the experimental setup for generating and maintaining levitated drops.

strength (500 MHz ^{1}H Larmor frequency) with a Bruker DSX 500 spectrometer, respectively. Standard Bruker microimaging hardware was used on both instruments, with birdcage resonators of either 10 mm (200 MHz) or 25 mm inner diameter (500 MHz). The microimaging units provided maximum gradient strengths of 1.0 T/m each.

2.3. Pulse sequences

Measurements of both systems were performed with the following strategy, each step being carried out on different drops beginning at the earliest possible moment after the drop generation. First, the positional and shape stability of the drops was verified by acquiring one-dimensional profiles in short succession (repetition time 200 ms) to cover particularly the settling time and the first few minutes of the drops' lives. Profiles were acquired along the vertical (z) as well as at least one of the horizontal (x, y) axes. Second, two- and three-dimensional images were obtained to visualize the drop's overall shape. Third, propagator measurements were performed to monitor the velocity distribution inside the drop in the three orthogonal directions. Because accumulation of impurities at the interface would be expected to affect the maximum occurring velocities, the total acquisition time of each propagator was reduced to the smallest possible value, in this case 40 s (4 scans). In the fourth and final step, velocity maps were obtained by supplementing fast imaging sequences with a velocity encoding module. The experiments were conducted either on individual slices inside the drop, or in an integral manner as a projection onto one plane, which, despite averaging over one dimension, still contained sufficient information about he velocity field to allow a comparison with available models. Measurement results with velocities encoded in orthogonal directions could then be combined to generate vector plots of the velocity fields.

Standard spin warp sequences were used for two- and three-dimensional imaging of toluene drops, while FLASH was applied for OMCTS. Propagator measurements were performed with pulsed gradient spin echo (PGSE) sequences where gradient duration and separation were set to $\delta = 1.0$ ms, $\Delta = 10$ ms, respectively.

The different spectra of the drop fluids, but also the vastly different velocities in the two types of drops required a suitable choice of encoding techniques to generate velocity maps in a minimal experimental time. In system I (OMCTS), the single spectral line and the relatively long relaxation times allowed the application of multiecho techniques. More important, however, were the small velocities which made possible a single velocity encoding prior to the imaging module. A RARE sequence had been employed in which the complete two-dimensional k space was covered in 64 phase encoding

steps without the need of segmentation. The sequence is shown in Fig. 2A. The duration of an individual acquisition step, consisting of the application of encoding phase, read, and rewinding phase gradient pulses, was 6 ms, leading to a total time of 384 ms for one RARE cycle. Typically, 128 scans were performed including phase-cycling, and 8 steps of the bipolar velocity encoding gradients were employed in order to allow a three-dimensional Fourier transformation with respect to k_{read}, k_{phase}, and q. This resulted in a propagator representation for each pixel, from which the local velocity was determined as the value of the maximum intensity of the propagator. The total duration of an encoding of one velocity component with a spatial resolution of 128×64 points was 20 min.

The multiline spectrum of the toluene leads to a multiplicity of images in the read dimension. To avoid this, the isolation of one particular spectral line is required. A frequency-selective rf pulse was thus used which excited
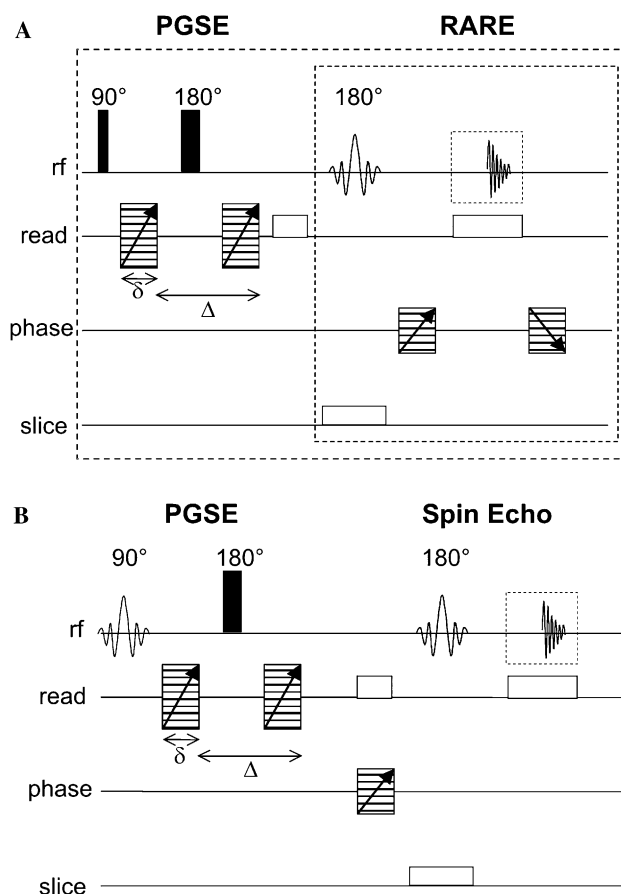

Fig. 2. Velocity imaging sequences employed in this study. (A) RARE-type imaging sequence preceded by a velocity encoding step, used for system I; for each PGSE step (outer box), a full RARE cycle was carried out (inner box). (B) Frequency-selective spin-echo type imaging sequence preceded by a velocity encoding step, used for system II; only one acquisition was made during each individual step and the sequence was repeated with the same velocity encoding value for each phase encoding step.

only the methyl line. Because of the much higher velocities expected for the toluene drop, a single velocity encoding followed by multiple signal acquisitions was not feasible: the requirement that the initially encoded spins must not travel farther than a distance equivalent to one pixel width (typically 117 μm) was not fulfilled for a multi-acquisition sequence. Therefore, a spin-echo imaging sequence was used, where each single acquisition was preceded by one velocity encoding step, and the whole succession of q and k encoding was repeated in typically 128 steps, corresponding to the spatial resolution in phase direction (see Fig. 2B). The repetition time was chosen as 200 ms with crusher gradients following each acquisition (not shown in figure) in order to destroy residual transverse magnetization persisting due to the long relaxation times of toluene of several seconds. Because of the longer experimental duration, usually only two velocity encoding steps were chosen and the local velocity was determined from the difference of the phase values in each pixel according to $\phi = 2\pi(q_2 - q_1)v\Delta$. Due to the smaller total number of signal accumulations, the results were found to be less accurate than the propagator technique mentioned above. The total duration of an encoding of one velocity component with a spatial resolution of 128×128 points was 4 min (without slice selection).

3. Results and discussion

3.1. System I: OMCTS drop

One-dimensional profiles of 2.7 mm diameter OMCTS drops were acquired every 200 ms to compute the stability in all three directions. The experiments consisted of a conventional spin-echo sequence with a read gradient applied in any of the three orthogonal directions, employing one scan each to avoid averaging. The experiments were begun at the time of the separation of the drop from the pipette, allowing the determination of the rise time until the drop had reached its final position near the centre of the resonator and had come to rest. The spatial resolution in these one-dimensional images was 20 μm.

It was found that once the drops reached their equilibrium position, they stabilized, and from the projections, time-invariant position and size could be deduced with an error of less than 1%, i.e., a possible variation in position along any of the axes was less than the spatial resolution of the profiles of 20 μm. The drops were almost perfectly spherical in shape, with a ratio between the axial and sagittal diameters of 1.01. Fig. 3 shows series of 512 projections acquired along the x and the z axis, respectively, covering intervals of 102 s each. In the first few lines of the z profiles, a change in the position and intensity of the profile is noticed which
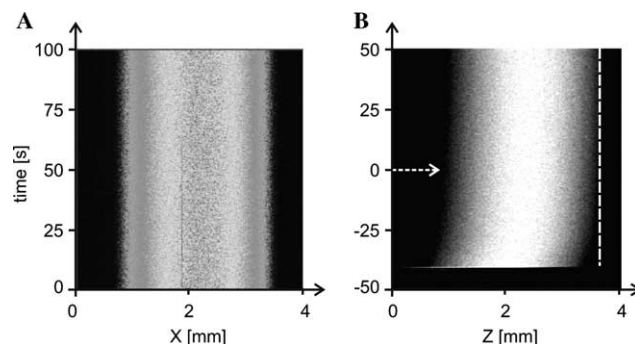

Fig. 3. Series of one-dimensional profiles for OMCTS drops: (A) along one horizontal (x) axis; (B) along the vertical (z) axis. 512 profiles each were acquired with a separation of 200 ms. For x profiles, the drop had already settled inside the resonator ($t = 0$ arbitrarily set at start of acquisition); measurements of the z profiles were started before so that the arrival of the drop at its final vertical position (indicated by the dashed line, set as $t = 0$) can be followed.

is a consequence of the drop moving into the resonator and approaching its final position. The drop then approaches its equilibrium position (dashed line) during a period of almost one minute.

To visualize the drop position with respect to the glass cell, the continuous D_2O phase was doped with a small amount of organic solvent to make the background signal detectable. A two-dimensional representation of the drop, projected onto the transverse (xy) plane is shown in Fig. 4. It can clearly be seen that the drop is located about 0.7 mm off the centre of this handmade cell which has subsequently been demonstrated to be asymmetric by means of 3D NMR imaging. This asymmetry did not affect the positional stability of the drop. It has, however, important consequences for the fluid dynamics because a net transverse component of the
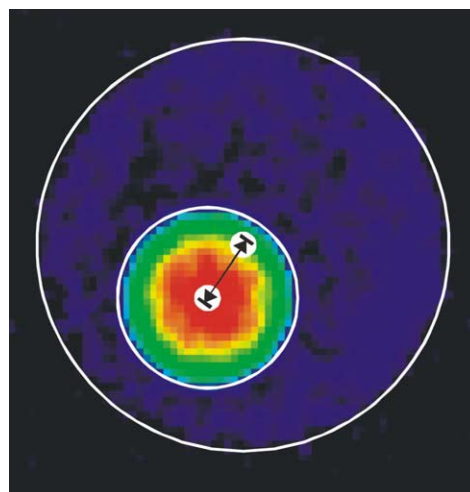

Fig. 4. Projection of the spin-density of an OMCTS drop onto the transverse (xy) plane. The continuous phase has been doped with proton-containing organic substances to enhance the signal. The drop centre is located 0.7 mm off the centre of the glass cell.

velocity of the continuous phase does exist under these circumstances. This complex problem was studied in more detail with a range of cells of different degrees of skewness but is outside the scope of this paper.

Propagator measurements were performed along all three spatial directions and at different 'drop ages' to monitor a possible change of the internal motion with time that would be expected from deposition of impurities at the interface. As can be seen from Fig. 5, velocities are in the range of 1 mm/s in every direction, much slower than the stream velocity of the continuous phase that is about 120 mm/s. No significant change of velocities was found for times of up to 72 h. An asymmetry can be identified along the x direction, but not, as might be expected, in the direction parallel to the counterflow, z. At the encoding time of $\Delta = 10$ ms used in these propagator experiments, self-diffusion accounts for an rms velocity of only about 0.25 mm/s so that internal motion certainly exists. In the extreme case of a perfectly 'rigid' interface, even these small velocity components should not occur. However, a completely immobile interface is not expected, and a more realistic assumption allows for a limited momentum transfer from the moving continuous phase across the interface to the drop phase. An overall rolling or tumbling motion is another possibility which needs to be considered.

To reveal the true nature of the internal motion, velocity imaging sequences of the type shown in Fig. 2A were applied to generate velocity maps along horizontal and vertical planes. Fig. 6 shows the distribution of individual velocity components in colour code for projections onto the horizontal plane (xy) and a vertical plane (zy), respectively. The left-most figure gives a clear indication of a rolling mechanism, where upward motion (positive v_z) in the right half of the drop takes place compared to downward motion (negative v_z) in its left half. The orientation of the axis about which rolling occurs cannot be defined to reasonable accuracy, but the absence of a similar pattern in other projections suggests that it is nearly horizontal. This can be understood from the drop position shown in Fig. 4 which allows not only for a transverse flow component hitting the drop,

but also demonstrates the existence of a velocity gradient of the continuous phase across the drop due to the different distances to the glass wall, where the flow velocity is bound to be zero.

The remaining three plots in Fig. 6 show more complicated velocity patterns. The second plot from the left visualizes the velocity component normal to the vertical plane which can clearly be separated into regions with motion into and out of the plane, respectively. The two plots on the right quantify the in-plane motion of the equatorial (horizontal) projection; here, positive v_x (motion "to the right") is dominating, while both positive and negative values of v_y are seen in well-distinct regions of the drop.

To visualize the internal drop dynamics more directly, an attempt was made to combine the measurements of two orthogonal velocity components in order to generate corresponding vector plots. The pulse sequences were performed with a slice-selective refocusing pulse that allowed the determination of velocity distributions in a slice of 340 μm thickness. Two central slices and the respective in-plane velocities are presented in Fig. 7; the location of the slices is indicated in the insets. The dominance of the rolling motion in the vertical plane becomes obvious from the left-hand part of Fig. 7. On the right-hand side, a vortex pattern is observed in the horizontal (equatorial) plane. This pattern is typical for fluid motion which is driven by momentum transfer from the continuous phase (see following section). The fact that the vortex occurs in horizontal direction indicates the important influence of the asymmetry of the velocity field outside the drop due to its off-centre position in the pipe. It should be noted that the maximum velocities found in the vector plot are comparable to those determined by the propagator technique and do not exceed 2 mm/s.

Velocity imaging experiments were repeated in different adjacent slices of 340 μm thickness each. The resulting patterns for the xy slices are shown in Fig. 8. The vortex structure appears in all plots. However, the vortex nodes are found to shift when travelling toward the poles of the drop. This indicates the presence of a more complex three-dimensional flow structure which, from comparing the available data along the principal planes, can be decomposed into two dominating contributions, a vortex that is approximated by a horizontal toroidal structure, superimposed onto a rolling motion about a horizontal axis. It is noteworthy to repeat that this pattern remains essentially unchanged over times of many hours or even days and thus represents a state of stability where internal and external forces are balanced, with negligible non-stationary effects being present.

3.2. System II: toluene drop

Toluene in water (D_2O) was chosen as an example for a fluid combination where density difference and interface
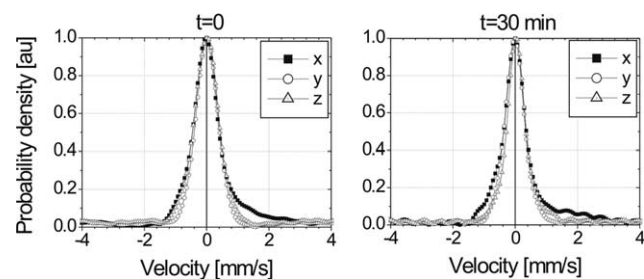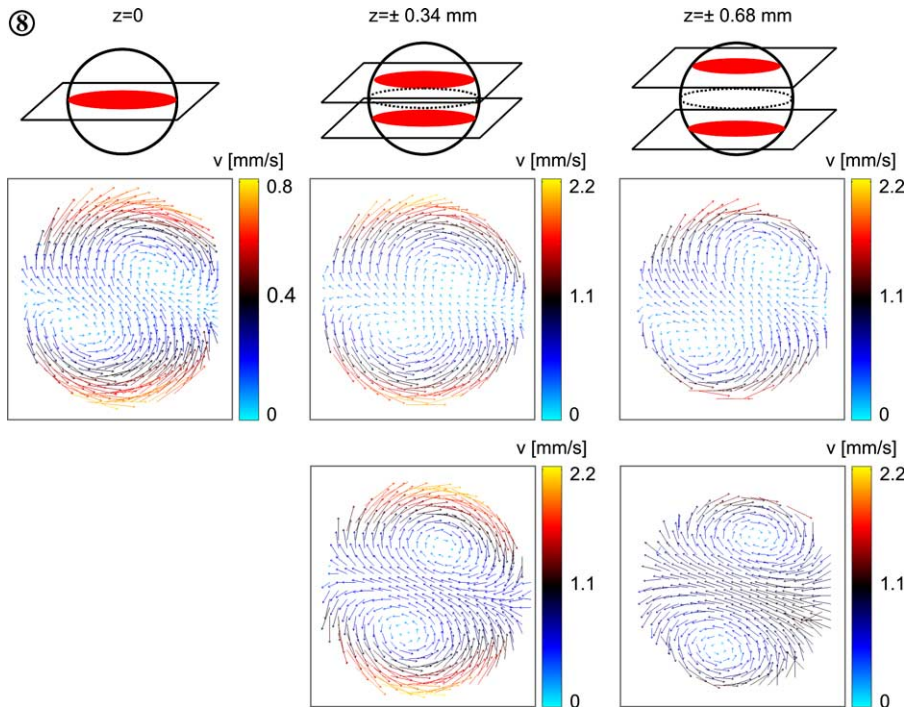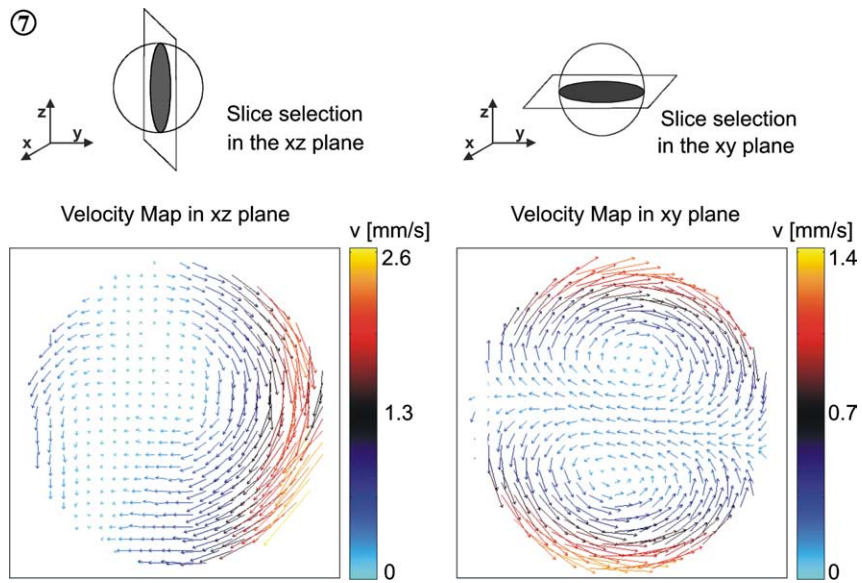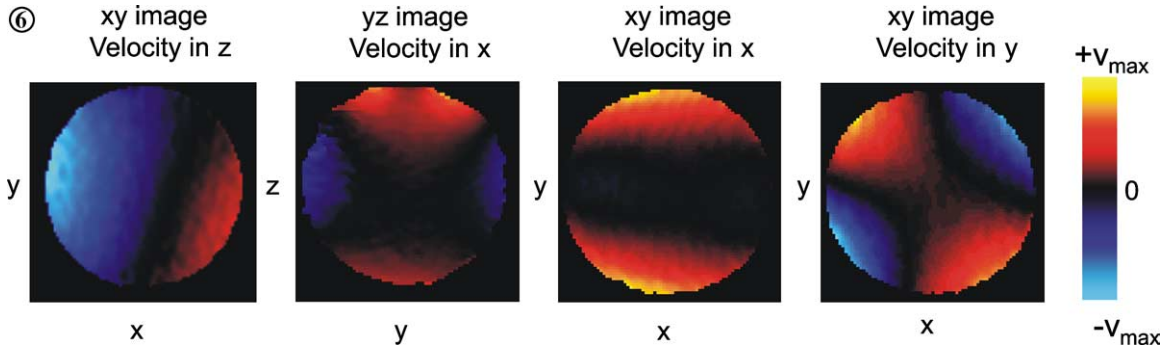
Fig. 5. Probability densities of velocities in three orthogonal directions for two different drop ages of OMCTS drops. Motion along the vertical axis is denoted v_z. The maximum values have been normalized to unity.

tension lead to the occurrence of a mobile interface for sufficiently large drops. To meet this criterion, drops of about 4 mm diameter were generated, because much larger sizes generally led to unstable drops or to collisions with the wall of the glass cell. All experiments on toluene drops were performed in the optimized glass cell (shown in Fig. 1) with a frequency-selective $\pi/2$ pulse of 2.0 ms duration centred on the methyl resonance that almost completely suppressed the signal of the aromatic protons.

The stability of the drop was confirmed with the same method as discussed above for the OMCTS drop, and the same stability tolerance was found once the drop had settled. The equilibrated toluene drop, however, possessed a non-spherical shape with an aspect ratio of 1.19, having an axial diameter of 3.6 mm and a sagittal diameter of 4.3 mm.

The results of the propagator measurements at different drop ages are presented in Fig. 9. As was expected, the velocities are now more than one order of magnitude larger as compared to the OMCTS drops, while the average velocity of the continuous phase near the drop position was similar at 160 mm/s. The highest velocities exceeded 30 mm/s in z direction, where an asymmetry is clearly observed, compared to almost symmetric velocity distribution functions of v_x and v_y. Despite this asymmetry, the average velocity in all three directions, obtained from integrating over the functions in Fig. 9, vanishes within experimental error. Although the mobile interface of the toluene drop should be more vulnerable to accumulated impurities, a significant change of the shape and width of the propagators was not observed for experiments carried out over a total time of 8 h. Moreover, no deviation could be determined between the velocity distributions obtained from several independent drops. Furthermore, repeated velocity images obtained for the same set-up revealed quantitatively similar, i.e., indistinguishable velocity patterns. This reproducibility is a strong hint that it is possible to generate drops with a pre-defined volume that possess identical velocity patterns, so that data can be directly compared or even superposed. This has important implications for future studies on mass-transfer where non-stationary conditions require the reconstruction of the desired image information from a series of individual drops.
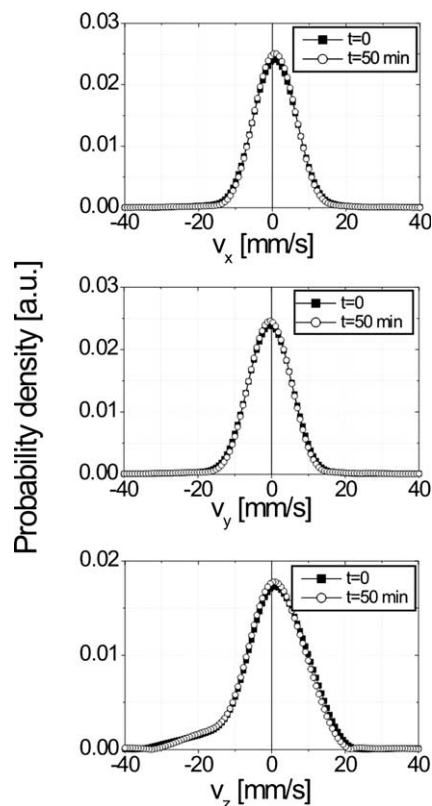

Fig. 9. Probability densities of velocities in three orthogonal directions for two different drop ages of toluene drops. Motion along the vertical axis is denoted v_z.

Slice-selective velocity images similar to those presented for OMCTS drops were also generated from toluene drops, but because of the need to use the conventional spin-echo technique, these measurements were much more time-consuming so that a comparable image quality could not yet be obtained. We will therefore present only two-dimensional images of the whole drop, which represent an integration over the remaining coordinate axis but are sufficient to reveal the internal vortex dynamics in a quantitative way. Fig. 10 summarizes the essential velocity patterns which are predicted for a drop with a mobile or partially mobile interface [7,8]. On the left-hand side, the different forces acting on the drop are shown. In the conical cell, the forces depend on the vertical (z) coordinate, leading to force balance at one

---

Fig. 6. Colour-coded plots of one velocity component each in a projection onto different planes of the OMCTS drop. The second plot from the left represents a projection onto the vertical (zy) plane, the remaining plots contain the three velocity components parallel to z, x, and y directions, respectively, projected onto the horizontal (xy) plane. The maximum velocities to which the plots are scaled are, from left to right, ±1, ±2, ±1.25, and ±1.25 mm/s, respectively.

Fig. 7. In-plane velocities in the central, 340 μm thick slice in vertical (left) and horizontal (right) orientation, respectively, of the OMCTS drop. The slice location is indicated in the accompanying sketches. Each vector was reconstructed from two single velocity encoding measurements (see Fig. 3A), carried out with gradients in orthogonal directions.

Fig. 8. As in this figure but for different horizontal slices of the same thickness 340 μm.
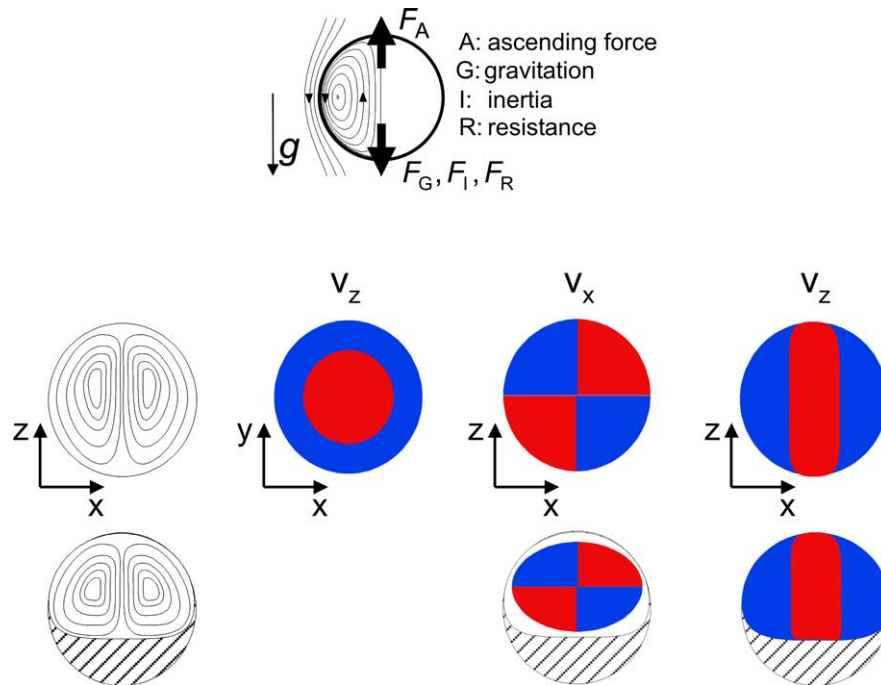
Fig. 10. Forces acting on the levitated drop (left) and schematic distribution of velocities by sign (red, positive; blue, negative). In the bottom line, the equivalent velocity distribution is shown for a drop with a rigid cap.

particular position. In the drop interior, a vortex is induced which can be most simply approximated by a toroidal velocity field. Similar vortices do exist in the exterior of the drop above a certain threshold Reynolds number [24,25]. The velocity distributions resulting from an integration along an axis perpendicular to the plane are drawn schematically in the remaining part of Fig. 10, where red indicates positive and blue, negative velocity components. Flow is directed upward in the centre, downward around the perimeter. The fountain-like trajectories lead to a cross-shaped pattern when the transverse velocities (here, v_x) are considered in a projection on a vertical plane.

In the bottom half of Fig. 10, the effect of a rigid cap in the drop is drawn. Such a cap has been described before as being the result of an incomplete interface mobil-
ity as a consequence of impurities or agents affecting the interface tension [7,8]. It appears at the downstream side of the drop which coincides with the drop's bottom half in this study as the flow direction of the continuous phase is from top to bottom. The rigid cap is, in principle, expected to grow with time if more impurities aggregate at the interface.

Fig. 11 shows the velocity maps of the drop. Due to the absence of slice selection, the velocity value in each pixel represents an integral over the projections along the remaining dimension which is normal to the plotted plane. The results agree qualitatively with the theoretical predictions, and considerably smaller velocities are visible in the bottom half of the vertical projections than in the top half (centre, right). To provide a better visualization of the internal drop dynamics, vector plots
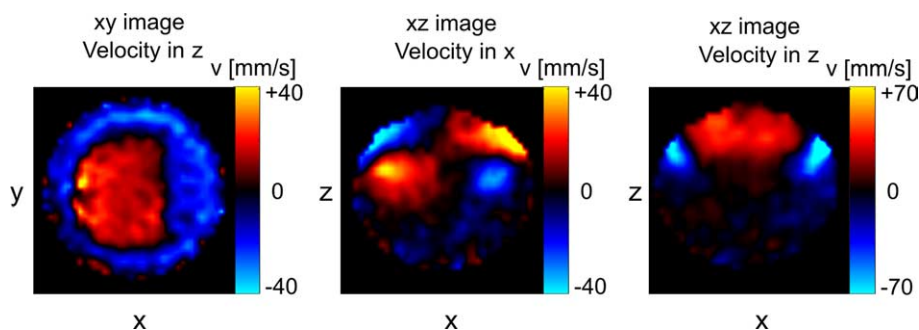

Fig. 11. Colour-coded plots of one velocity component each in a projection on different planes of the toluene drop; velocity components and plane orientations are given in the figure.

have been reconstructed by the same method described earlier but lacking the slice selection. In Fig. 12, these vector plots are shown. The circulation (vortex) pattern is restricted to approximately the upper half of the drop, while typically 10 times smaller velocities occur in the bottom half. They do not show a particular feature and appear to be random; however, this might be a consequence of the volume averaging which can mask an existing regular pattern. The horizontal projection, on the other hand, reveals an indistinct velocity distribution which is expected as all 'outward' and 'inward' flowing fluid elements would compensate when viewed from the top, with a small asymmetry brought about by the rigid cap which deforms the toroidal velocity

field. A vortex-like pattern with small residual velocity components of below 3 mm/s is indeed found in the right-hand part of Fig. 12.

To demonstrate the sensibility of the technique, a final test was made by tilting the whole cell deliberately. Assuming a rigid rod, the geometrical constraints by the inner magnet bore and the fixations allowed a tilt angle of less than 0.2°, but a possible bending of the glass tube could have led to a somewhat larger tilt angle that could not be determined directly. Under these circumstances, the drop must experience a superposition of internal vortex and overall rolling motions which add up linearly in the measured velocity field. However, because of the presence of the rigid cap that rests in place
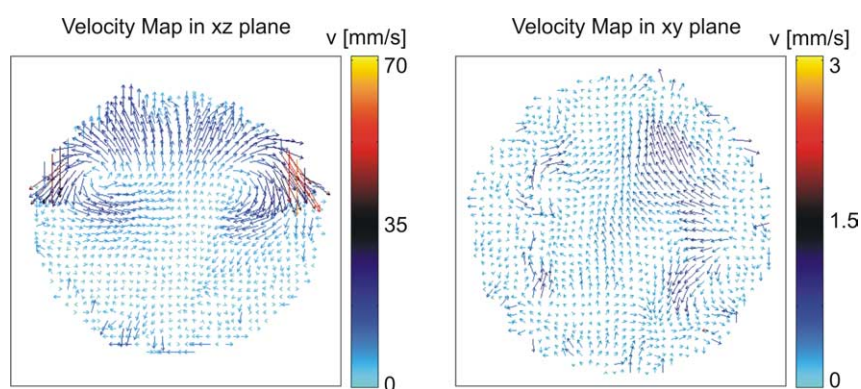

Fig. 12. Vector plots of the internal velocities in a toluene drop averaged over the dimension normal to the drawing plane. Left, vertical projection; right, horizontal projection.
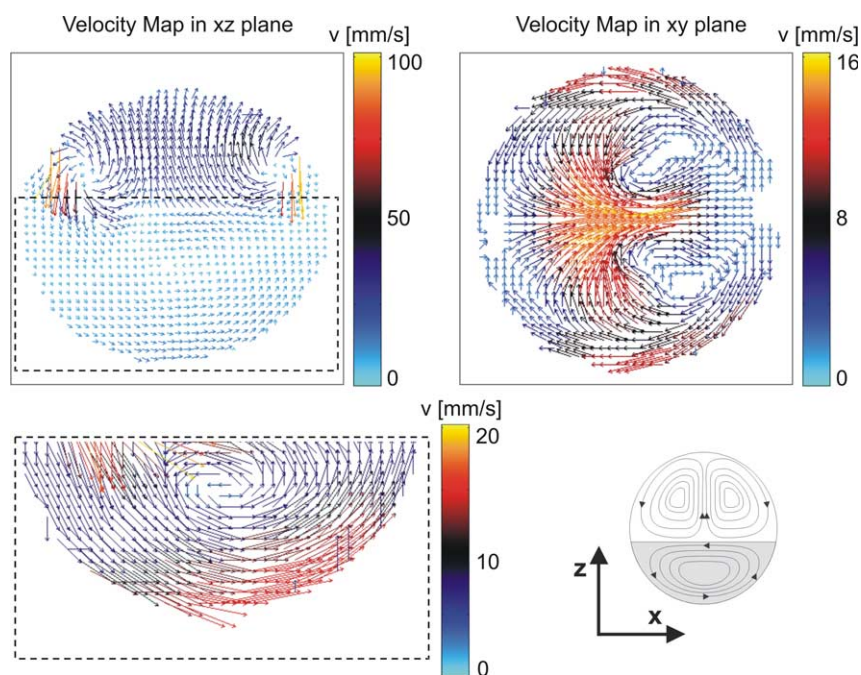

Fig. 13. Vector plots of the internal velocities in a toluene drop in an asymmetric stream environment, averaged over the dimension normal to the drawing plane. Top left, vertical projection; bottom left, lower part of the drop with arrow lengths increased fivefold; top right, horizontal projection; bottom right, sketch of principal flow pattern (not to scale).

at the bottom of the drop, the internal dynamics becomes more complicated than such a mere superposition. At the same time, the aspherical drop is not found to tumble as a whole which would be easily observable by a variation of its axis length. Instead, its shape is preserved and the asymmetric flow of the continuous phase leads to a more complex internal circulation that can qualitatively be understood from the vector plots of Fig. 13. While the vortex in the upper half remains the dominating feature, a circulating pattern becomes visible in the lower half (left-hand plot in Fig. 13, vector lengths increased fivefold for a better comparison in the inset at bottom). The projection onto the horizontal plane (right-hand plot) reveals a remarkable asymmetric vortex pattern containing relatively large velocity components. From the magnitude of the additional velocities observed in this drop, a rotation velocity of about 10 mm/s can be estimated, corresponding to roughly one rotation per second.

4. Conclusions

Several devices were constructed which served for the controlled levitation, i.e., localization in space, of liquid drops in a second, immiscible liquid phase. By using one-dimensional NMR imaging, it could be shown that drops of different substances could be stabilized with accuracies better than 20 μm, which has not been demonstrated by available optical methods before. The internal velocity field of OMCTS (silicone oil) and toluene drops were measured by different velocity encoding imaging schemes. In all cases, a stable pattern was revealed for times of hours or even days, which hints to the fact that continuing contamination of the drop interface did not affect the hydrodynamics significantly, but inherent impurities of the system had an influence on the internal flow pattern. This was particularly well observed by the occurrence of a rigid cap next to a vortex region inside toluene drops with an overall mobile interface. OMCTS drops, on the other hand, revealed a similar internal circulation pattern but with a much reduced velocity range. All drops were found to be reproducible in shape and dynamic properties, which provides possibilities for future applications to monitor the influence of mass-transfer of a third fluid component at low concentrations.

In the context of this work, fast imaging techniques were combined with velocity encoding modules that allowed the reconstruction of three-dimensional velocity fields within small objects at a resolution that is high with respect to both space and velocity. Their combination with chemical-shift selective pulses represents a promising step for the in situ monitoring of processes where the coupling of reaction and transport need to be treated simultaneously.

References

[1] R. Kronig, J.C. Brink, On the theory of extraction from falling droplets, Appl. Sci. Res. A 2 (1950) 142.

[2] E. Gross-Hardt, M. Henschke, A. Pfennig, Letter to the Editor, AIChE J. 49 (2003) 1611.

[3] M.A. Waheed, M. Henschke, A. Pfennig, Simulating sedimentation of liquid drops, Int. J. Num. Methods Eng. 59 (2004) 1821.

[4] M. Henschke, A. Pfennig, Mass-transfer enhancement in single-drop extraction experiments, AIChE J. 45 (1999) 2079.

[5] M. Henschke, Auslegung pulsierter Siebboden—Extraktionskolonnen, Habilitationsschrift RWTH Aachen, Shaker Aachen, 2004.

[6] P. Savic, Internal circulation inside drops, Nat. Res. Counc. Can. Rep. MT-22 (1953).

[7] J.T. Davis, Turbulence Phenomena, Academic Press, New York/London, 1972.

[8] R. Clift, J.R. Grace, M.E. Weber, Bubbles, Drops and Particles, Academic Press, New York, 1978.

[9] E. Fukushima, Nuclear magnetic resonance as a tool to study flow, Ann. Rev. Fluid Mech. 31 (1999) 95.

[10] J. Hennig, A. Nauerth, H. Friedburg, RARE imaging: a fast imaging method for clinical MR, Magn. Reson. Med. 3 (1986) 823.

[11] P. Mansfield, P.G. Morris, NMR imaging in biomedicine, Adv. Magn. Res. (Suppl. 2) 1982.

[12] A. Haase, J. Frahm, D. Matthei, W. Hänicke, K.D. Merboldt, FLASH imaging: rapid NMR imaging using low flip-angle pulses, J. Magn. Reson. 67 (1986) 258.

[13] A.J. Sederman, M.D. Mantle, C. Buckley, L.F. Gladden, MRI technique for measurement of velocity vectors, acceleration, and autocorrelation functions in turbulent flow, J. Magn. Reson. 166 (2004) 182.

[14] M. Rokitta, U. Zimmermann, A. Haase, Fast NMR flow measurements in plants using FLASH imaging, J. Magn. Reson. 137 (1999) 29.

[15] T.W.J. Scheenen, D. van Dusschoten, P.A. de Jager, H. Van As, Microscopic displacement imaging with pulsed field gradient turbo spin–echo NMR, J. Magn. Reson. 142 (2000) 207.

[16] R.W. Mair, C.H. Tseng, G.P. Wong, D.G. Cory, R.L. Walsworth, Magnetic resonance imaging of convection in laser-polarized xenon, Phys. Rev. E 61 (2000) 2741.

[17] S. Han, P.T. Callaghan, One-shot velocimetry using echo planar imaging microscopy, J. Magn. Reson. 148 (2001) 349.

[18] M. Klarhofer, B. Csapo, C. Balassy, J.C. Szeles, E. Moser, High-resolution blood flow velocity measurements in the human finger, Magn. Reson. Med. 45 (2001) 716.

[19] W.R. Overall, D.G. Nishimura, B.S. Hu, Fast phase-contrast velocity measurement in the steady state, Magn. Reson. Med. 48 (2002) 890.

[20] B. Manz, Combined relaxation and displacement experiment: a fast method to acquire T_2, diffusion and velocity maps, J. Magn. Reson. 169 (2004) 60.

[21] B. Newling, C.C. Poirier, Y. Zhi, J.A. Rioux, A.J. Coristine, D. Roach, B.J. Balcom, Velocity imaging of highly turbulent gas flow, Phys. Rev. Lett. 93 (2004) 154503.

[22] S. Han, S. Stapf, B. Blümich, NMR imaging of falling water drops, Phys. Rev. Lett. 87 (2001) 144501.

[23] E. Gross-Hardt, E. Slusanschi, H.M. Bücker, A. Pfennig, C.H. Bischof, Practical Shape Optimization of a Levitation Device for Single Droplets, Opt. Eng. (submitted).

[24] S. Taneda, Experimental investigation of the wakes behind cylinders and plates at low Reynolds numbers, J. Phys. Soc. Jpn. 11 (1956) 302.

[25] V.G. Jenson, Viscous flow round a sphere at low Reynolds numbers (<40), Proc. R. Soc. Lond. A. 249 (1959) 346.